ACS APPLIED MATERIALS & INTERFACES



Organic Electronic Devices

# Probe and Control of the Tiny Amounts of Dopants in BHJ Film Enable Higher-Performance Polymer Solar Cells

Zhenyu Chen, Yabing Tang, Baojun Lin, Hanzhang Zhao, Tao Li, Tai Min, Han Yan, and Wei Ma

*ACS Appl. Mater. Interfaces*, **Just Accepted Manuscript** • DOI: 10.1021/acsami.0c06127 • Publication Date (Web): 07 May 2020

# Probe and Control of the Tiny Amounts of Dopants in BHJ Film Enable Higher-Performance Polymer Solar Cells

*Zhenyu Chen,*[†] *Yabing Tang,*[†] *Baojun Lin,*[†] *Hanzhang Zhao,*[‡] *Tao Li,*[‡] *Tai Min,*[‡] *Han Yan,*[*,†] *Wei Ma*[*,†]

[†] State Key Laboratory for Mechanical Behavior of Materials, Xi'an Jiaotong University, Xi'an, 710049, P. R. China

[‡] Center of Spintronics and Quantum Systems, State Key Laboratory for Mechanical Behavior of Materials, School of Materials Science and Engineering, Xi'an Jiaotong University, Xi'an, 710049, P. R. China

KEYWORDS: Polymer solar cell, molecular doping, n-type doping, doped morphology, ternary blend solar cell

ABSTRACT: In order to achieve efficient doping in polymer solar cell (PSC), the dopant needs to be selectively located in the binary components of bulk heterojunction (BHJ) film according to its polarity. The rarely studied n-type dopant is thoroughly examined in a simplified planar heterojunction (PHJ) device to address its favored location in the active layer. Results show that the n-dopant distributing in the acceptor layer or at the donor/acceptor interface produces enhanced device performance, whereas it harms the device when locating in the donor layer. Based on the results, the benefit of n-type doping is then transferred to the high-efficient BHJ devices via a sequential coating procedure. The performance improvement is closely linked with the variation of dopant's location in the BHJ film, which is carefully examined by the synchrotron techniques with delicate chemical sensitivity. More interestingly, the sequential coating procedure can be easily extended to the p-doped device only by changing the dopant's polarity in the middle layer. These findings pave the way of ambipolar doping in PSCs and make performance improvement by molecular doping within expectation.

## INTRODUCTION

The power conversion efficiency of PSC is dominated by steps of charge generation and collection. In theory, the electronic properties of organic semiconductors determine the loss of the photovoltaic process.[1-3] As a widely used strategy, molecular doping modifies the electronic properties of organic semiconductors through tuning the electronic structures at working interfaces and shaping the density of states at specific energies.[4-6] The control of these fundamental electronic properties has been found vital to improve the performances of organic light-emitting diodes (OLEDs),[7,8] organic field-effect transistors (OFETs),[9-14] and organic thermoelectric devices (OTEs),[15,16] and also displays attractive potential for PSC.[17-26] The active

layer of PSC is made of interpenetrating networks of the electron donor and acceptor, which is named as the BHJ structure.[27] The binary components at nanoscale guarantee efficient free charge generation and transportation. The unique BHJ structure proposes a new challenge for efficient doping in PSC, which is the well-controlled doping polarity in different components. Taking the p-type doping as an example, it reduces the charge recombination and optimizes the BHJ morphology when the p-dopants locate in the donor phase.[18-20,23,28,29] It is also reported that the p-type doping facilitates photo-charge generation when the dopants distribute at the donor/acceptor heterojunction.[21,30,31] The n-type doping is assumed to work in similar mechanisms for PSCs, although it is yet rarely reported.[23,32] Consequently, the gap between molecular doping and the cell performance lies in the selective dopant's location for both of p-type and n-type doping in the BHJ film.

The difficulties in achieving the controlled dopant's location in the BHJ film manifest in two aspects, the lack of the ability to detect the dopants in various components and the complex film formation process. The low chemical contrast between the molecular dopant and organic semiconductor due to similar atomic compositions inhibits probing the tiny amount of dopants. Usually, people are blind to the dopant's distribution in the BHJ film. In the solution process, the dopant's location in the BHJ film can be pre-determined in solution or formed during morphological evolution. When molecular doping takes place via integer charge transfer (ICT) between the dopant and host material in solution, the bounded ion pair will lock the ionized dopant in the desired domain.[33-35] Nevertheless, ICT is prohibited by several factors in the PSC devices, including the insufficient energy offset,[36,37] the un-avoided donor-acceptor molecular structure,[38] the twisted molecular conformation,[39] the heated solution temperature,[34] and the poor

dopant/component miscibility.[40-42] Given these circumstances, an emergent study on the doped BHJ solar cell should enable us observing and controlling the dopant's location.

In a PHJ device structure, the donor and acceptor are well stacked via sequential procedure.[43,44] In this case, the dopant can be well confined in various controlled locations, including the donor layer, the acceptor layer, and the donor-acceptor heterojunction.[21,26] Apparently, the knowledge of the PHJ devices provide a simple way to deduce the dopant's location compared to the BHJ devices. Furthermore, a synchrotron based technique, the resonant soft X-ray scattering (R-SoXS) is a promising tool to directly probe the dopant in the BHJ film. The R-SoXS is an optical characterizing methods based on the differences in material's refractive index in soft X-ray region.[45,46] It is applicable to distinguish organic compounds with low chemical contrast, and has obtained numerous success in the BHJ PSCs.[47-50] For the control of dopant's location in the BHJ film, the dopant and the component with opposite charge polarity can be pre-separated via a layer-by layer coating process.[51,52] The pre-defined phase separation is designed to exclude the dopant from the wrong phase. The undesired component is deposited first, and the dopant is added in a second step. The doped PSC device is fabricated by coating a top layer of the rest component. The doping type of the cell is supposed to be controlled by the dopant's polarity in the middle layer.

In this contribution, we report a sequential coating procedure, which is applicable to both types of doping in PSCs. The rarely studied n-type doped cell is taken as an example to screen the influence of dopant's location on photovoltaic performance in PHJ devices. The results point out that the n-type dopants locating at the donor/acceptor heterojunction or in the acceptor layer are efficient to improve the device performance. The benefits of n-type doping are then transferred into the BHJ devices by sequential coating procedure. The dopant's distribution is

inferred from the PHJ results and detected by the R-SoXS measurements in the blend films. These measurements convincingly relate the enhanced performance to the favored dopant's location. Furthermore, the procedure is extended to fabricate the p-type doped cell. The rational control of dopant's location is a key to fully exploiting the doping benefits in PSCs, and we believe that it will lead to a performance improvement across a wide range of material systems.

## RESULTS AND DISCUSSION

We explore the selectivity of n-type dopant's location in BHJ film with the aid of a simplified PHJ device structure. We use (4-(1,3-dimethyl-2,3-dihydro-1H-benzoimidazol-2-yl) phenyl)dimethylamine (N-DMBI)[9,53,54] as an n-type dopant, and add it in three different locations of the poly[4,8-bis(5-(2-ethylhexyl)-thiophene-2-yl)benzo[1,2-b;4,5-b']dithiophene-2,6-diyl-alt-(4-(2-ethylhexyl)-3-fluorothieno[3,4-b]thiophene-)-2-carboxylate-2-6-diyl]] (PTB7-Th)/a fused octacylic electron acceptor (FOIC) bilayer,[55] including the PTB7-Th layer, the FOIC layer, and the heterojunction of PTB7-Th/FOIC. The chemical structures of the stuffs are listed in **Figure 1a**. The n-type doping effect on FOIC was confirmed by Kelvin probe force microscopy (KPFM) in **Figure S1**. To obtain a well-defined PHJ structure, the PTB7-Th/FOIC PHJ cells in inverted structure was fabricated according to our previous reports.[21,26] The current density versus voltage (*J-V*) curves of the PHJ solar cells at each optimum condition are plotted in **Figure 1b**, and the device parameters are summarized in **Table 1**. More detailed data are referenced in **Table S1-S3**. It seems that N-DMBI doping almost equally improves the cell performance when it distributes in the FOIC layer or at the PTB7-Th/FOIC heterojunction. Adding N-DMBI in the FOIC layer of PHJ device produces a short-circuit current ($J_{sc}$) increase from 5.36 mA/cm$^2$ to above 5.60 mA/cm$^2$ (**Figure 1b**), which is supported by the external quantum efficiency (EQE) measurements (**Figure S2**). Together with a slightly better fill factor (FF) and a constant open-

circuit voltage ($V_{oc}$), the overall PCE increases from 2.91% to 3.08%. Locating the N-DMBI at the PTB7-Th/FOIC heterojunction produces a similar PCE value of 3.06%. The results of PHJ devices demonstrate the importance of N-DMBI's distribution to cell performance, however the correct distribution will not spontaneously form during the BHJ formation.

In the blend solution of PTB7-Th/FOIC/N-DMBI, the dopant content is actually quite low. Taking a typical doping content of 0.01 wt% as an example, the absolute concentration of N-DMBI is merely 0.001 mg/mL in chlorobenzene (CB), which is 10,000 times lower than PTB7-Th. Assuming that the N-DMBI precipitates much later than the liquid-liquid (L-L) phase separation between PTB7-Th and FOIC, its distribution is mutually determined by the material-solvent interactions and the extent of morphological evolution.[56,57] The material-solvent interaction can be intuitively deduced from the ternary phase diagram of CB/PTB7-Th/FOIC (**Figure 1c**), and the calculation of ternary phase diagram is described in our previous work.[26] The binodal line is derived at the chemical potential equilibrium of two liquid phases, below it, the L-L phase separation is triggered. The material-solvent interaction is manifested by the tie lines. If the left side of the tie lines is higher than the right side, CB resides more in the PTB7-Th rich phase; otherwise, CB resides more in the FOIC rich phase. The extent of morphological evolution can be roughly estimated by the film formation time due to its dynamic essence. We measure the spin-coating and drop-casting film formation time by in-situ reflection spectroscopy (**Figure 1d**). The short time of 2.3 s to 193.0 s reveals that the morphology of spin-coated film in device fabrication is far from the thermodynamic equilibrium. The kinetic process hinders the morphological evolution, which is visualized to the much smaller phase separation in the spin-coated film (**Figure 1e and f**). In this situation, CB tends to carry more N-DMBI into the PTB7-Th rich phase, because the morphology is freezed at low quenching depth in the ternary phase

diagram (**Figure 1c**). Apparently, the wrong distribution of N-DMBI hinders the effective n-type doping in BHJ devices.

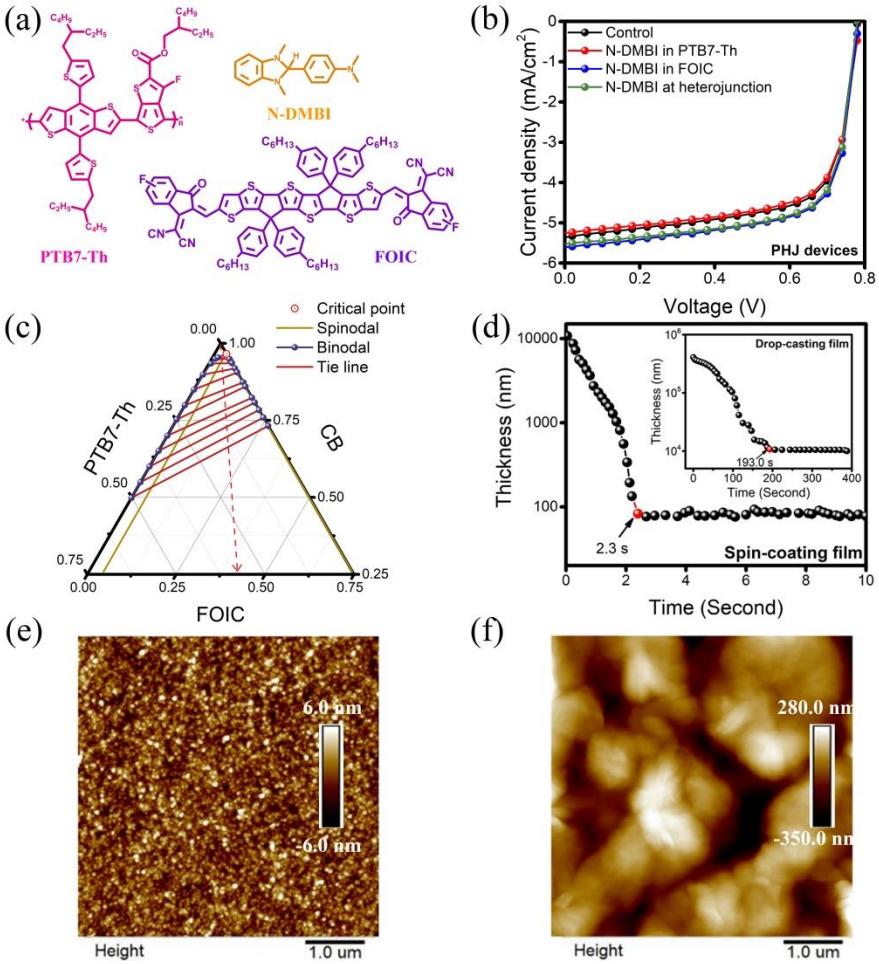


**Figure 1.** (a) The chemical structures of PTB7-Th, FOIC, and N-DMBI. (b) Photovoltaic performances of PTB7-Th/FOIC in PHJ device structure. The 'control' represents un-doped device, the 'N-DMBI in PTB7-Th' contains 0.001 wt% N-DMBI, the 'N-DMBI in FOIC' contains 0.01 wt% N-DMBI, and the 'N-DMBI at heterojunction' is coated by 0.0001 mg/mL N-DMBI ethanol solution. (c) Ternary phase diagram of PTB7-Th, FOIC, and CB. The region inside the spinodal line is of complete instability; the binodal line is the boundary between the single phase region and the metastable region; the tie lines connect the compositions with equal chemical potentials; the critical point is the intersection of both the binodal line and the spinodal line; the red arrow is the solvent quenching line, indicting the compositional variation of blend solution during solvent quenching. (d) In-situ thickness measurements of the spin-coating and drop-casting PTB7-Th/FOIC films. (e, f) AFM images of PTB7-Th/FOIC films via different film formation procedures: (e) spin-coating; (f) drop-casting.

**Table 1.** Photovoltaic performances of PTB7-Th/FOIC in PHJ device structure corresponding to Figure 1b.[a)]

| Conditions | $V_{oc}$ max (V) | $J_{sc}$ max (mA/cm$^2$) | $J_{sc}$ avg (mA/cm$^2$) | $FF_{max}$ (%) | $FF_{avg}$ (%) | $PCE_{max}$ (%) | $PCE_{avg}$ (%) |
|---|---|---|---|---|---|---|---|
| Control | 0.78 | 5.36 | 5.35±0.04 | 68.5 | 68.6±0.41 | 2.91 | 2.89±0.01 |
| N-DMBI in PTB7-Th | 0.78 | 5.26 | 5.32±0.07 | 68.4 | 67.7±0.57 | 2.86 | 2.84±0.02 |
| N-DMBI in FOIC | 0.78 | 5.60 | 5.63±0.06 | 69.7 | 69.5±0.27 | 3.08 | 3.06±0.02 |
| N-DMBI at heterojunction | 0.78 | 5.53 | 5.64±0.05 | 70.1 | 69.1±0.52 | 3.06 | 3.04±0.02 |

[a)]Average value of 15 devices fabricated under identical conditions ±1 standard deviation.

To obstruct the N-DMBI infiltration into the PTB7-Th rich domain, we propose a sequential coating procedure instead of the one-step coating procedure from blend solution. As schemed in **Figure 2a**, PTB7-Th and N-DMBI were spin-coated on the cathode substrate separately from the orthogonal solvents of CB and ethanol to form a distinct bilayer structure. Then FOIC was deposited from CB onto the N-DMBI layer to form a doped sequential-coating BHJ (Seq_BHJ) film. The predefined PTB7-Th/N-DMBI phase separation was partially preserved after their fast dissolving in CB. We propose that the prior phase separation overcomes the insufficient L-L phase separation between PTB7-Th and N-DMBI, thus hinders N-DMBI entering the PTB7-Th rich phase.

Our hypothesis on the modified N-DMBI's location via different coating procedures was proved by the photovoltaic testing. Based on the statistical data, adding N-DMBI in blend solution doesn't improve the device performance (**Figure 2b** and **c**, and **Table S4**). Although the $V_{oc}$ and $J_{sc}$ increase a bit, the suppressed FF compromise the overall device performance of the control and 0.01 wt% doped devices (**Table 2**). Further increasing the N-DMBI's content negatively affects the PCE value. Fabricating devices via the sequential coating procedure, we obtain slightly higher PCE value in the control sample. Importantly, when we spin-coat a middle layer of N-DMBI in 0.01 mg/mL ethanol solution, the maximum PCE increases from 10.14% to

11.21% (**Figure 2d** and **e**, **Table 2**, and **Table S5**). The N-DMBI doping in Seq_BHJ devices leads to $J_{sc}$ raising from 21.68 mA/cm$^2$ to 23.08 mA/cm$^2$, at the same time the FF increases from 62.7% to 65.8%. These phenomena are well consistent with the PHJ device results, where the PCE improvement is directly related to the N-DMBI's location in the active layer.

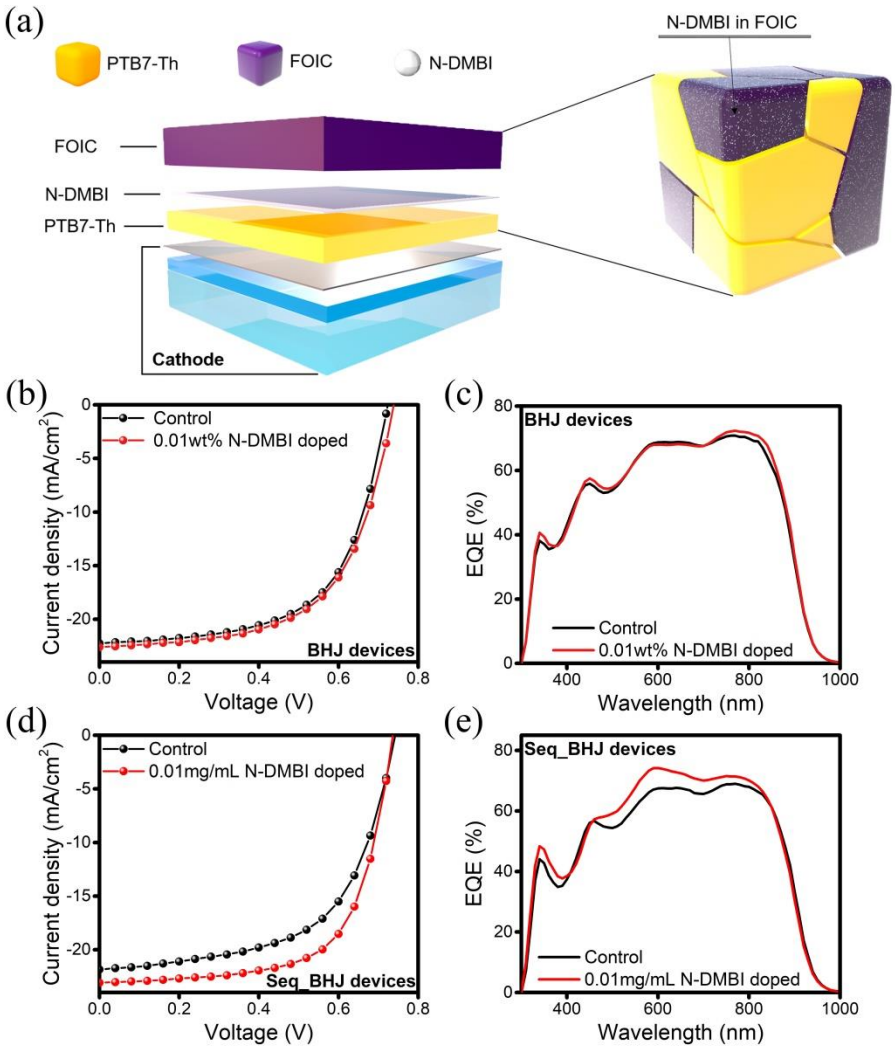


**Figure 2.** (a) Scheme of the sequential coating process and the corresponding model of doped Seq_BHJ film. (b, c) Photovoltaic performances of PTB7-Th/FOIC fabricated by one-step spin-coating: (b) *J–V* curves; (c) corresponding EQE curves. (d, e) Photovoltaic performances of PTB7-Th/FOIC fabricated by sequential spin-coating: (d) *J–V* curves; (e) corresponding EQE curves.

**Table 2.** Photovoltaic performances of PTB7-Th/FOIC in BHJ device structure.[a)]

| Device Structure | Conditions | $V_{oc}$ max (V) | $J_{sc}$ max ($mA/cm^2$) | $J_{sc}$ avg ($mA/cm^2$) | $FF_{max}$ (%) | $FF_{avg}$ (%) | $PCE_{max}$ (%) | $PCE_{avg}$ (%) |
|---|---|---|---|---|---|---|---|---|
| BHJ | Control | 0.72 | 22.26 | 22.37±0.22 | 60.8 | 60.8±0.75 | 9.96 | 9.90±0.06 |
| | 0.01 wt% | 0.74 | 22.60 | 22.72±0.19 | 59.8 | 59.7±0.77 | 10.01 | 9.88±0.06 |
| Seq_BHJ | Control | 0.74 | 21.68 | 21.58±0.38 | 62.7 | 62.8±0.66 | 10.14 | 9.92±0.13 |
| | 0.01 mg/mL | 0.74 | 23.08 | 22.77±0.43 | 65.8 | 65.0±0.94 | 11.21 | 10.98±0.11 |

[a)] Average value of 15 devices fabricated under identical conditions ±1 standard deviation.

Aside from the electronic doping, the morphological optimization, especially the enhanced crystallinity, is always the explanation for improved cell performance in PSCs. To distinguish the role of n-type doping from the morphological optimization, we thoroughly examined the BHJ and Seq_BHJ structures by grazing incidence wide-angle X-ray scattering (GIWAXS).[58] The (010) peaks representing the π-π stacking locate at 1.62 $Å^{-1}$ for PTB7-Th and 1.83 $Å^{-1}$ for FOIC (**Figure S3**). The obviously stronger peak intensity in the out of plane direction suggests that both of PTB7-Th and FOIC adopt face-on orientation to the substrate in the blend films. Furthermore, the addition of N-DMBI doesn't change the molecular orientation in the blend films (**Figure 3**). The corresponding coherence length (CL) is then fitted to evaluate the crystallinity change after N-DMBI addition. In the BHJ films, the CLs of PTB7-Th and FOIC coincidently decrease when adding N-DMBI. The values decrease from 9.9 Å to 9.5 Å for PTB7-Th, and decrease from 31.4 Å to 30.7 Å for FOIC. In the Seq_BHJ films, the CL variations of PTB7-Th and FOIC appear opposite. The CLs increase from 9.6 Å to 10.4 Å for PTB7-Th, while decrease from 31.9 Å to 27.7 Å for FOIC. This is consistent with the assumption that more N-DMBI distributes in the FOIC rich phase, which disturbing the crystallinity of FOIC. Considering the d-spacing of π-π stacking is 3.88 Å and 3.43 Å for PTB7-Th and FOIC, the rather small CL enhancement of 0.8 Å in PTB7-Th is barely responsible for the PCE

enhancement in the Seq_BHJ film. After the detailed analysis by GIWAXS, we exclude the improved crystallinity as the reason for better photovoltaic performance, hence we confirm the importance of n-type doping in our study.

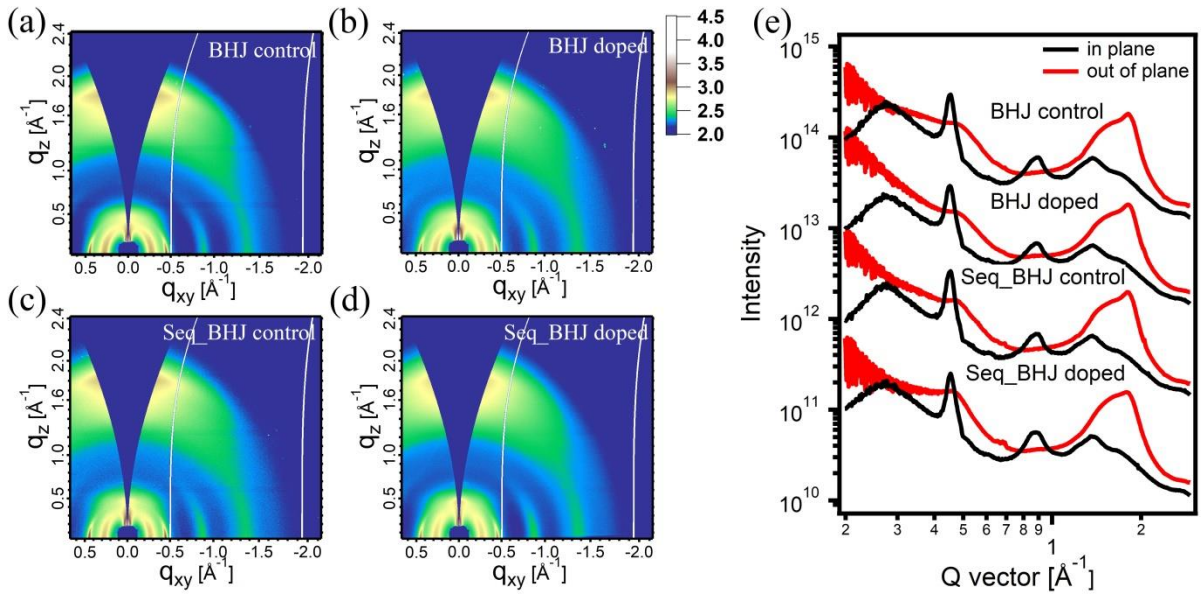


**Figure 3.** (a, b) Two-dimensional GIWAXS patterns of BHJ films: (a) Control; (b) 0.01 wt% N-DMBI doped. (c, d) Two-dimensional GIWAXS patterns of Seq_BHJ films: (c) Control; (d) 0.01 mg/mL N-DMBI doped. (e) The corresponding in plane and out of plane line cuts of the GIWAXS patterns.

To better understand the different situations in the N-DMBI doped BHJ and Seq_BHJ films, herein, we look into more direct evidence for the locations of N-DMBI in various components. The difficulty on probing the N-DMBI's distribution lies in its low content and weak chemical contrast in the PTB7-Th/FOIC blend film. Recently, R-SoXS has been popular to distinguish chemical compounds from multi-component organic systems.[46,59,60] By tuning the X-ray photon energy matched with the absorption edge of constituent element, unique sensitivity correlating with molecular structure is obtained. The chemical contrast comes from the differences in energy-dependent index of refraction, and it is expressed as $C_{12}(E)=E^4\{[\delta_1(E)-\delta_2(E)]^2+[\beta_1(E)-\beta_2(E)]^2\}$, where δ and β are the real and imaginary indices of refraction, and E is the X-ray

photon energy.[59,60] The δ and β of PTB7-Th, FOIC, and N-DMBI are plotted in **Figure 4a** and **b**, which are derived from the near edge X-ray absorption fine structure (NEXAFS) spectroscopy. The pairwise scattering contrasts are calculated correspondingly and depicted in **Figure 4c**. The maximum contrast locates at 284.8 eV for PTB7-Th/FOIC and FOIC/N-DMBI, while PTB7-Th/N-DMBI displays low contrast in the whole range of X-ray photon energy. According to the relations in **Figure 4a** and **b**, the addition of N-DMBI in FOIC will decrease the R-SoXS scattering contrast. We observe the decreased scattering signal with the addition of N-DMBI in the Seq_BHJ film, which is in sharp contrast to the overlapped scattering curves in the BHJ samples (**Figure 4d**). These observations clearly reveal that more N-DMBI entering the FOIC rich phase by the sequential coating procedure. Since we are unable to give the accurate N-DMBI's distribution in the FOIC rich phase, we cannot further evaluate the relative importance of bulk doping and heterojunction doping. In general, we think both are responsible for the positive device performance. We also compare the nanoscale phase separation in the BHJ and Seq_BHJ samples by fitting the peak position. The higher scattering peak with low q position demonstrates that the Seq_BHJ film has larger extent of phase separation than the BHJ film, which is also clearly visualized by the tapping-mode atomic force microscopy (**Figure S4**). This is expected by the predefined phase separation between PTB7-Th and FOIC via sequential coating. From the AFM images, we also notice that the addition of N-DMBI doesn't alter the size order of phase separation between the BHJ and Seq_BHJ films. The doped Seq_BHJ film still shows larger extent of phase separation than the doped BHJ film, which is consistent with the R-SoXS results. As expected, we are unable to see the dopants in AFM images. We stress that the larger domain with higher purity suppresses the N-DMBI interpenetration into the PTB7-Th rich phase, thus it corrects the wrong N-DMBI's distribution in the BHJ film. The N-DMBI's

location in the Seq_BHJ film was further confirmed by the photoluminescence (PL) spectra. Opposite effects of N-DMBI are observed: the dopant quenches the PL intensity of FOIC, while unexpectedly enhances the PL intensity of PTB7-Th (**Figure 4e**). In the Seq_BHJ films, N-DMBI doping quenches the PL intensity (**Figure 4f**), which proves that more N-DMBI distributes in the FOIC rich phase.

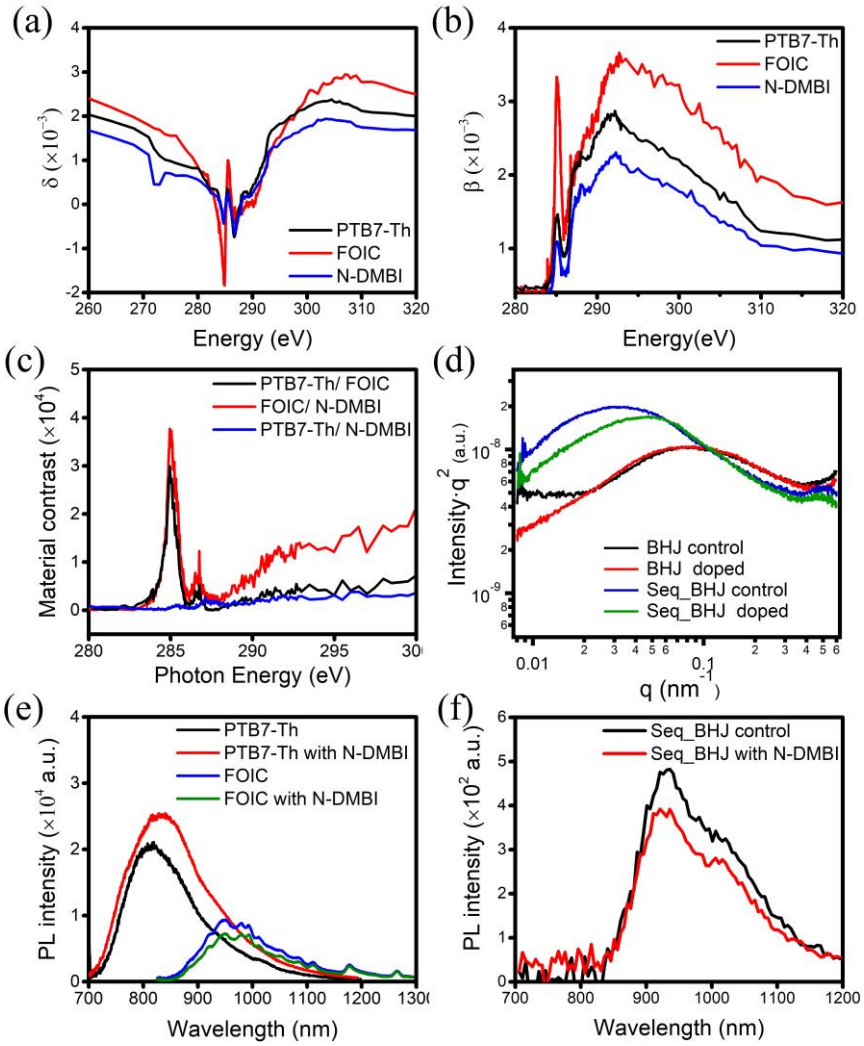


**Figure 4.** (a, b) Real (δ) and imaginary (β) part of the complex index of refraction of PTB7-Th, FOIC, and N-DMBI. (c) Pairwise material contrast calculating from the δ and β. (d) Corresponding R-SoXS profiles probing at 284.8 eV. (e, f) Photoluminescence spectra recorded using 695 nm (PTB7-Th and Seq_BHJ film) and 806 nm (FOIC film) excitation. The N-DMBI contents are 1 wt% for single component films in PL measurement. All the samples of blend

films are fabricated in the real device condition, and the N-DMBI contents are chosen according to the best performance.

After successful n-type doping the PSCs, we further explore the potential of p-type doping by the sequential coating procedure. A typical p-type dopant, tris(pentafluorophenyl)borane (BCF), is chosen in our study.[61,62] The optimum BCF's location for photovoltaic performance was examined in the PHJ device structure (**Figure 5a** and **b**, **Table 3**, and **Table S6-S8**). The doped devices achieve best performance when BCF locates at the heterojunction of PTB7-Th/FOIC. The improved performance is due to the enhanced $J_{sc}$ from 5.36 mA/cm$^2$ to 5.80 mA/cm$^2$, making the overall PCE value increases from 2.91% to 3.12%. Fixing BCF in the PTB7-Th layer also brings $J_{sc}$ increase to 5.50 mA/cm$^2$ with a PCE value of 3.04%. In the BCF doped PHJ devices, the heterojunction doping outperforms the bulk doping. These results describe a different model that more BCF should locate at the PTB7-Th/FOIC heterojunction to maximize the doping effect. Since the predefined S-S phase separation between PTB7-Th and BCF help exclude BCF from PTB7-Th rich phase, the only problem here is how to further inhibit BCF infiltrating into the FOIC rich phase. Fortunately, the fluorinated chemical structure of BCF has a small Hildebrand solubility parameter of 16.3 MPa$^{1/2}$ comparing to N-DMBI of 23.6 MPa$^{1/2}$, which makes it immiscible with FOIC (25.9 MPa$^{1/2}$) and PTB7-Th (20.9 MPa$^{1/2}$) (**Table S9**). Thus spontaneous phase separation between BCF and FOIC is thermodynamically favored during the FOIC coating step. The Seq_BHJ device doped by 0.001 mg/mL BCF solution successfully enhance the $J_{sc}$ from 21.68 mA/cm$^2$ to 22.77 mA/cm$^2$. Together with the FF increase from 62.7% to 65.5%, the maximum PCE raises from 10.14% to 10.94% (**Figure 5c** and **d**, **Table 3**, and **Table S10**).

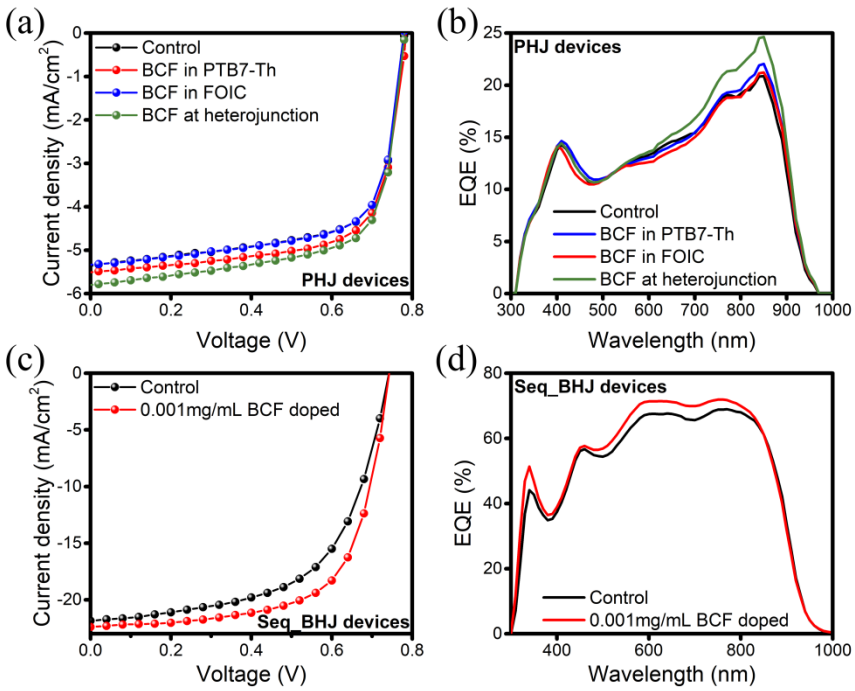


**Figure 5.** (a) Photovoltaic performances of PTB7-Th/FOIC in PHJ device structure. (b) Corresponding EQE spectra of the PTB7-Th/FOIC in PHJ device structure. The 'control' represents un-doped device, the 'BCF in PTB7-Th' contains 0.01 wt% N-DMBI, the 'BCF in FOIC' contains 0.001 wt% N-DMBI, and the 'BCF at heterojunction' is coated by 0.0001 mg/mL N-DMBI ethanol solution. (c, d) Photovoltaic performances of PTB7-Th/FOIC fabricated by sequential spin-coating: (c) J–V curves; (d) corresponding EQE curves.

**Table 3.** Photovoltaic performances of PTB7-Th/FOIC in PHJ and Seq_BHJ device structure corresponding to Figure 5.[a)]

| Device Structure | Conditions | $V_{oc}$ max (V) | $J_{sc}$ max (mA/cm$^2$) | $J_{sc}$ avg (mA/cm$^2$) | $FF_{max}$ (%) | $FF_{avg}$ (%) | $PCE_{max}$ (%) | $PCE_{avg}$ (%) |
|---|---|---|---|---|---|---|---|---|
| PHJ | Control | 0.78 | 5.36 | 5.35±0.04 | 68.5 | 68.6±0.41 | 2.91 | 2.89±0.01 |
| | BCF in PTB7-Th | 0.78 | 5.50 | 5.60±0.07 | 69.5 | 68.0±0.13 | 3.04 | 3.00±0.05 |
| | BCF in FOIC | 0.78 | 5.33 | 5.31±0.01 | 68.8 | 68.5±0.28 | 2.87 | 2.85±0.02 |
| | BCF at heterojunction | 0.78 | 5.80 | 5.62±0.10 | 68.8 | 69.3±0.35 | 3.12 | 3.08±0.03 |
| Seq_BHJ | 0.001 mg/mL | 0.74 | 22.77 | 22.48±0.22 | 65.5 | 65.3±0.55 | 10.94 | 10.80±0.18 |

[a)] Average value of 15 devices fabricated under identical conditions ±1 standard deviation.

## CONCLUSION

In summary, we have demonstrated that the key to fulfill the doping benefit in PSCs is the rationally controlled dopant's location in the BHJ blend film. In contrast to the devices

fabricating from the doped blend solution, the n-type doped devices via triple-layer coating procedure get obviously better device performance. We attribute the efficient n-type doping to the correct dopant's location. The pre-deposited donor/dopant double layers enable complete phase separation, hence they force n-type dopants distributing more in the acceptor rich phase after the third layer coating. The direct evidence of n-type dopant's location in the blend film comes from the R-SoXS and PL measurements, where the complex index of refraction and charge-transfer provide sufficient contrast to probe the ultralow content of n-type dopant. The reduced R-SoXS intensity and PL quenching clarify that the n-type dopants reside in the acceptor rich phase via sequential coating procedure. We also fabricate the p-type doped cells by changing the dopant's polarity in the middle layer. Therefore, we expect this methodology to become a practical tool for the ambipolar doped PSCs in the future.

## EXPERIMENTAL SECTION

***Materials:*** PTB7-Th and FOIC were purchased from Solarmer Materials Inc. N-DMBI, BCF, zinc acetate dihydrate, ethanolamine, 2-methoxyethanol, and Zirconium acetylacetonate (ZrAcac) were purchased from Sigma-Aldrich.

***Device Fabrication*:** The PHJ devices were fabricated with a configuration of ITO/ZnO/FOIC/PTB7-Th/$MoO_X$/Al. The BHJ devices were fabricated with a configuration of ITO/PEDOT:PSS/PTB7-Th:FOIC/ZrAcac/Al. The ITO substrates were cleaned by sequential sonication and plasma treatment. The electron-transporting layer of ZnO was deposited by spin-coating a ZnO precursor solution (dissolving zinc acetate in 2-methoxyethanol with ethanolamine) at 4500 rpm for 30s, followed by thermal annealing at 200 °C for 30 min. The film-transfer layer of PEDOT:PSS for PHJ devices was deposited by spin-coating at 2000 rpm for 30s, followed by thermal annealing at 150 °C for 2 min. The hole-transporting layer of

PEDOT:PSS for BHJ devices was deposited by spin-coating at 5500 rpm for 30s, followed by thermal annealing at 150 °C for 20 min. The PHJ devices were fabricated according to our recently published process in reference 17 and 22. BHJ devices were fabricated by spin-coating PTB7-Th/FOIC blend solution or sequentially spin-coating each single component in the $N_2$ glove box. Finally, 10 nm $MoO_3$/100 nm Al or 20 nm ZrAcac/100 nm Al were deposited as the electrode at a vacuum level of < $1\times10^{-5}$ Pa.

***Instrumentation:*** The apparatus for morphology characterization (AFM, KPFM, reflectance spectra, GIWAXS, and R-SoXS), photovoltaic performance measurements (*J–V* curves, EQE curves and UV–vis absorption spectra), and the film thickness testing are accessible in reference 15, 17, and 22. PL spectrum was recorded by FLS980 spectrometer (Edinburgh Instruments, EI) with different excitation wavelength.

***NEXAFS characterization:*** NEXAFS spectroscopy was conducted at beamline 5.3.2 Advanced Light Source (ALS). The NEXAFS samples were spin-coated on PEDOT:PSS glass substrates and then transferred to copper grid by floating in water. For the measurement, a 200μm × 200μm image scan was first run under 320 eV to find the film edge. Then move the cursor to a proper position which is supposed to contain both film and vacuum. A focus scan was then made across the film edge and set the cursor on focus. Use smaller size range to repeat the image scan as well as focus scan until 20 μm × 20 μm. Move line cursor across the film edge to do the energy scan from 270 eV to 320 eV. The material contrast between two pure materials can be calculated from the absorption spectra.

ASSOCIATED CONTENT

**Supporting Information**.

The Supporting information is available free of charge on ACS Publication website at DOI:

KPFM images; EQE spectra of PHJ devices; GIWAXS patterns; AFM Graphics; Detailed photovoltaic performances for PHJ and BHJ devices; Parameters for calculation of the Flory-Huggins interaction parameters (χ). (PDF)

AUTHOR INFORMATION

**Corresponding Author**

* E-mail: mseyanhan@xjtu.edu.cn (H.Y.).

* E-mail: msewma@xjtu.edu.cn (W.M.).

**Author Contributions**

The manuscript was written through contributions of all authors. All authors have given approval to the final version of the manuscript.

**Funding Sources**

This work was supported by the Ministry of Science and Technology of China, National Natural Science Foundation of China.

**Notes**

The authors declare no competing financial interest.

ACKNOWLEDGMENT

Thanks for the support from Ministry of science and technology (2016YFA0200700), National Natural Science Foundation of China (21975198, 51803162, 21875182), the Fundamental Research Funds for the Central Universities (Z201805178), and 111 project 2.0 (BP2018008).

ABBREVIATIONS

PSC, polymer solar cell

BHJ, bulk heterojunction

PHJ, planar heterojunction

OLEDs, organic light-emitting diodes

OFETs, organic field-effect transistors

OTEs, organic thermoelectric devices

ICT, integer charge transfer

R-SoXS, resonant soft X-ray scattering

N-DMBI, (4-(1,3-dimethyl-2,3-dihydro-1H-benzoimidazol-2-yl) phenyl)dimethylamine

PTB7-Th, poly[4,8-bis(5-(2-ethylhexyl)-thiophene-2-yl)benzo[1,2-b;4,5-b']dithiophene-2,6-diyl-alt-(4-(2-ethylhexyl)-3-fluorothieno[3,4-b]thiophene-)-2-carboxylate-2-6-diyl]]

KPFM, Kelvin probe force microscopy

$J_{sc}$, short-circuit current

EQE, external quantum efficiency

$V_{oc,}$ open-circuit voltage

PCE, power conversion efficiency

FF, fill factor

CB, chlorobenzene

Seq_BHJ, sequential-coating BHJ

GIWAXS, grazing incidence wide-angle X-ray scattering

CL, coherence length

NEXAFS, near edge X-ray absorption fine structure

PL, photoluminescence

BCF, tris(pentafluorophenyl)borane

REFERENCES

(1) Benduhn, J.; Tvingstedt, K.; Piersimoni , F.; Ullbrich, S.; Fan, Y.; Tropiano, M.; McGarry, K. A.; Zeika, O.; Riede, M. K.; Douglas, C. J.; Barlow, S.; Marder, S. R.; Neher, D.; Spoltore, D.; Vandewal, K. Intrinsic Non-Radiative Voltage Losses in Fullerene-Based Organic Solar Cells. *Nat. Energy* **2017**, *2*, 1-6.

(2) Menke, S. M.; Ran, N. A.; Bazan, G. C.; Friend, R. H. Understanding Energy Loss in Organic Solar Cells: Toward A New Efficiency Regime. *Joule* **2018**, *2*, 25-35.

(3) Nakano, K.; Chen, Y.; Xiao, B.; Han, W.; Huang, J.; Yoshida, H.; Zhou, E.; Tajima, K. Anatomy of The Energetic Driving Force for Charge Generation in Organic Solar Cells. *Nat. Commun.* **2019**, *10*, 1-10.

(4) Salzmann, I.; Heimel, G.; Oehzelt, M.; Winkler, S.; Koch, N. Molecular Electrical Doping of Organic Semiconductors: Fundamental Mechanisms and Emerging Dopant Design Rules. *Acc. Chem. Res.* **2016**, *49*, 370-378.

(5) Jacobs, I. E.; Moulé, A. J. Controlling Molecular Doping in Organic Semiconductors. *Adv. Mater*. **2017**, *29*, 1703063.

(6) Gaul, C.; Hutsch, S.; Schwarze, M.; Schellhammer, K. S.; Bussolotti, F.; Kera, S.; Cuniberti, G.; Leo, K.; Ortmann, F. Insight into Doping Efficiency of Organic Semiconductors from The Analysis of The Density of States in n-Doped C60 and ZnPc. *Nat. Mater*. **2018**, *17*, 439-444.

(7) Gross, M.; Müller, D. C.; Nothofer, H.-G., Scherf, U.; Neher, D.; Bräuchle, C.; Meerholz, K. Improving The Performance of Doped P-Conjugated Polymers for Use in Organic Light-Emitting Diodes. *Nature* **2000**, *405*, 661-665.

(8) Pfeiffer, M.; Leo, K.; Zhou, X.; Huang, J. S.; Hofmann, M.; Werner, A.; Nimoth, J. B-.; Doped Organic Semiconductors: Physics and Application in Light Emitting Diodes. *Org. Electron*. **2003**, *4*, 89-103.

(9) Wei, P.; Oh, J. H.; Dong, G.; Bao, Z. Use of a 1H-Benzoimidazole Derivative as An N-Type Dopant and To Enable Air-Stable Solution-Processed n-Channel Organic Thin-Film Transistors. *J. Am. Chem. Soc*. **2010**, *132*, 8852-8853.

(10) Han, Y.; Barnes, G.; Lin, Y.-H.; Martin, J.; Al-Hashimi, M. Doping of large ionization potential indenopyrazine polymers via lewis acid complexation with tris (pentafluorophenyl) borane: a simple method for improving the performance of organic thin-film transistors. *Chem. Mater.* **2016**, *28*, 8016-8024.

(11) Panidi, J.; Paterson, A. F.; Khim, D.; Fei, Z.; Han, Y.; Tsetseris, L.; Vourlias, G.; Patsalas, P. A.; Heeney, M.; Anthopoulos, T. D. Remarkable Enhancement of the Hole Mobility in Several Organic Small-Molecules, Polymers, and Small-Molecule:Polymer Blend Transistors by Simple Admixing of the Lewis Acid p-Dopant $B(C_6F_5)_3$. *Adv. Sci.* **2018**, *5*, 1700290.

(12) Xu, Y.; Sun, H.; Liu, A.; Zhu, H.; Li, W.; Lin, Y.; Noh, Y. Doping: A Key Enabler for Organic Transistors. *Adv. Mater*. **2018**, *30*, 1801830.

(13) Panidi, J.; Kainth, J.; Paterson, A. F.; Wang, S.; Tsetseris, L.; Emwas, A.-H.; Mclachlan, M. A.; Heeney, M.; Anthopoulos, T. D. Introducing a Nonvolatile N-Type Dopant Drastically Improves Electron Transport in Polymer and Small-Molecule Organic Transistors. *Adv. Funct. Mater*. **2019**, *29*, 1902784.

(14) Paterson, A.F.; Tsetseris, L.; Li, R.; Basu, A.; Faber, H.; Emwas, A.-H.; Panidi, J.; Fei, Z.; Niazi, M R.; Amjum, D H.; Heeney, M.; Anthopoulos, T D. Addition of the Lewis Acid $Zn(C_6F_5)_2$ Enables Organic Transistors with a Maximum Hole Mobility in Excess of 20 $cm^2 V^{-1} s^{-1}$. *Adv. Mater.* **2019**, *31*, 1900871.

(15) Kim, G-H.; Shao, L.; Zhang, K.; Pipe, K. P. Engineered Doping of Organic Semiconductors for Enhanced Thermoelectric Efficiency. *Nat. Mater*. **2013**, *12*, 719-723.

(16) Russ, B.; Glaudell, A.; Urban, J. J.; Chabinyc, M. L.; Segalman, R. A. Organic Thermoelectric Materials for Energy Harvesting and Temperature Control. *Nat. Rev. Mater.* **2016**, *1*, 1-14.

(17) Zhang, Y.; Zhou, H.; Seifter, J.; Ying, L.; Mikhailovsky, A.; Heeger, A. J.; Bazan, G. C.; Nguyen, T. -Q. Molecular Doping Enhances Photoconductivity in Polymer Bulk Heterojunction Solar Cells. *Adv. Mater*. **2013**, *25*, 7038-7044.

(18) Yan, H.; Manion, J. G.; Yuan, M.; Arquer, F. P. G.; McKeown, G. R., Beaupré, S.; Leclerc, M.; Sargent, E. H., Seferos, D. S. Increasing Polymer Solar Cell Fill Factor by Trap-Filling with F4TCNQ at Parts Per Thousand Concentration. *Adv. Mater*. **2016**, *28*, 6491-6496.

(19) Yan, H.; Chen, J.; Zhou, K,; Tang, Y.; Meng, X.; Xu, X.; Ma, W. Lewis Acid Doping Induced Synergistic Effects on Electronic and Morphological Structure for Donor and Acceptor in Polymer Solar Cells. *Adv. Energy Mater.* **2018**, *8*, 1703672.

(20) Xiong, Y.; Ye, L.; Gadisa, A.; Zhang, Q.; Rech, J. J.; You, W.; Ade, H. Revealing The Impact of F4TCNQ as Additive on Morphology And Performance of High-Efficiency Nonfullerene Organic Solar Cells. *Adv. Funct. Mater*. **2019**, *29*, 1806262.

(21) Yan, H.; Tang, Y.; Sui, X.; Liu, Y.; Gao, B.; Liu, X.; Liu, S. F.; Hou, J.; Ma, W. Increasing Quantum Efficiency of Polymer Solar Cells with Efficient Exciton Splitting and Long Carrier Lifetime by Molecular Doping at Heterojunctions. *ACS Energy Lett*. **2019**, *4*, 1356-1363.

(22) Yu, S.; Yang, Q.; Yu, W.; Zhang, J.; Liu, J.; Jin, S.; Guo, X.; Li, C. Performance Enhancement of Ternary Polymer Solar Cells Induced by Tetrafluorotetracyanoquinodimethane Doping. *Chem. Mater*. **2019**, *31*, 7650-7656.

(23) Lin, Y.; Firdaus, Y.; Nugraha, M. I.; Liu, F.; Karuthedath, S.; Emwas, A.-H.; Zhang, W.; Seitkhan, A.; Neophytou, M.; Faber, H.; Yengel, E.; McCulloch, I.; Tstseris, L.; Laquai, F.; Anthopoulos, T. D. 17.1% Efficient Single-Junction Organic Solar Cells Enabled by n-Type Doping of The Bulk-Heterojunction. *Adv. Sci*. **2020**, *7*, 1903419.

(24) Zhang, D.; Li, Q.; Zhang, J.; Wang, J.; Zhang, X.; Wang, R.; Zhou, J.; Wei, Z.; Zhang, C.; Zhou, H.; Zhang, Y. Control of Nano- morphology in Fullerene-Free Organic Solar Cells by Lewis Acid Doping with Enhanced Photovoltaic Efficiency. *ACS Appl. Mater. Interfaces.* **2020**, *12*, 667-677.

(25) Yan, H.; Tang, Y.; Meng, X.; Xiao, T.; Lu, G.; Ma, W. Achieving High Doping Concentration by Dopant Vapor Deposition in Organic Solar Cells. *ACS Appl. Mater. Interfaces.* **2019**, *11*, 4178-4184.

(26) Tang, Y.; Lin, B.; Zhao, H.; Li, T.; Ma, W.; Yan, H. Significance of Dopant/Component Miscibility to Efficient n-Doping in Polymer Solar Cells. *ACS Appl. Mater. Interfaces.* **2020**, *12*, 13021-13028.

(27) Yu, G.; Gao, J.; Hummelen, J. C.; Wudl, F.; Heeger, A. J. Polymer Photovoltaic Cells: Enhanced Efficiencies via A Network of Internal Donor-Acceptor Heterojunctions. *Science* **1995**, *270*, 1789-1791.

(28) Loiudice, A.; Rizzo, A.; Biasiucci, M.; Gigli, G. Bulk Heterojunction Versus Diffused Bilayer: The Role of Device Geometry in Solution p-Doped Polymer-Based Solar Cells. *J. Phys. Chem. Lett*. **2012**, *3*, 1908-1915.

(29) Shang, Z.; Heumueller, T.; Prasanna, R.; Burkhard, G. F.; Naab,B. D.; Bao, Z.; McGehee, M. D.; Salleo, A. Trade-Off between Trap Filling, Trap Creation, and Charge Recombination Results in Performance Increase at Ultralow Doping Levels in Bulk Heterojunction Solar Cells. *Adv. Energy Mater*. **2016**, *6*, 1601149.

(30) Deschler, F.; Como, E. Da.; Limmer, T.; Tautz, R.; Godde, T.; Bayer, M.; Hauff, E. von.; Yilmaz, S.; Allard, S.; Scherf, U.; Feldmann, J. Reduced Charge Transfer Exciton Recombination in Organic Semiconductor Heterojunctions by Molecular Doping. *Phys. Rev. Lett*. **2011**, *107*, 127402.

(31) Tunc, A. V.; De Sio, A.; Riedel, D.; Deschler, F.; Da Como, E.; Parisi, J.; von Hauff, E. Molecular Doping of Low-Bandgap-Polymer: Fullerene Solar Cells: Effects on Transport and Solar Cells. *Org. Electron*. **2012**, *13*, 290-296.

(32) Xu, Y.; Yuan, J.; Sun, J.; Zhang, Y.; Ling, X.; Wu, H.; Zhang, G.; Chen, J.; Wang, Y.; Ma, W. From PCBM-Polymer to Low-Cost and Thermally Stable C60/C70-Polymer Solar Cells: The Role of Molecular Structure, Crystallinity, and Morphology Control. *ACS Appl. Mater. Interfaces.* **2018**, *10*, 24037-24045.

(33) Duong, D. T.; Wang, C.; Antono, E.; Toney, M. F.; Salleo, A. The Chemical and Structural Origin of Efficient p-Type Doping in P3HT. *Org. Electron*. **2013**, *14*, 1330-1336.

(34) Duong, D. T.; Phan, H.; Hanifi, D.; Jo, P. S.; Nguyen, T.-Q.; Salleo, A. Direct Observation of Doping Sites in Temperature-Controlled, p-Doped P3HT Thin Films by Conducting Atomic Force Microscopy. *Adv. Mater.* **2014**, *26*, 6069-6073.

(35) Jacobs, I. E.; Aasen, E. W.; Olivera, J. L.; Fonseca, T. N.; Roehling, J. D.; Li, J.; Zhang, G.; Augustine, M. P.; Mascal, M.; Moulé, A. J. Comparison of Solution-Mixed and Sequentially Processed P3HT: F4TCNQ films: Effect of Doping-Induced Aggregation on Film Morphology. *J. Mater. Chem. C.* **2016**, *4*, 3454-3466.

(36) Méndez, H.; Heimel, G.; Opitz, A.; Sauer, K.; Barkowski, P.; Oehzelt, M.; Soeda, J.; Okamoto, T.; Takeya, J.; Arilin, J.-B.; Balandier, J.-Y. ; Geerts, Y.; Koch, N.; Salzmann, I. Doping of Organic Semiconductors: Impact of Dopant Strength and Electronic Coupling. *Angew. Chem. Int. Ed*. **2013**, *52*, 7751-7755.

(37) Méndez, H.; Heimel, G.; Winkler, S.; Frisch, J.; Opitz, A.; Sauer, K.; Wegner, B.; Oehzelt, M.; Röthel, C.; Duhm, S.; Többens, D.; Koch, N.; Salzmann, I. Charge-Transfer Crystallites as Molecular Electrical Dopants. *Nat. Commun.* **2015**, *6*, 1-11.

(38) Di Nuzzo, D.; Fontanesi, C.; Jones, R.; Allard, S.; Dumsch, I.; Scherf, U.; von Hauff, E.; Schumacher, S.; Da Como, E. How Intermolecular Geometrical Disorder Affects the Molecular Doping of Donor-Acceptor Copolymers. *Nat. Commun*. **2015**, *6*, 1-8.

(39) Gao, J.; Niles, E. T.; Grey, J. K. Aggregates Promote Efficient Charge Transfer Doping of Poly (3-hexylthiophene). *J. Phys. Chem. Lett.* **2013**, *4*, 2953-2957.

(40) Schlitz, R. A.; Brunetti, F. G.; Glaudell, A. M.; Miller, P. L.; Brady, M. A.; Takacs, C. J.; Hawker, C. J.; Chabinyc, M. L. Solubility-Limited Extrinsic n-type Doping of A High Electron Mobility Polymer for Thermoelectric Applications. *Adv. Mater.* **2014**, *26*, 2825-2830.

(41) Liu, J.; Qiu, L.; Portale, G.; Koopmans, M.; Brink, G.; Hummelen, J. C.; Koster, L. J. A. N-Type Organic Thermoelectrics: Improved Power Factor by Tailoring Host-Dopant Miscibility. *Adv. Mater*. **2017**, *29*, 1701641.

(42) Qiu, L.; Liu, J.; Alessandri, R.; Qiu, X.; Koopmans, M.; Havenith, R. W. A.; Marrink, S. J.; Chiechi, R. C.; Koster, L. J. A.; Hummelen, J. C. Enhancing Doping Efficiency by Improving Host-Dopant Miscibility for Fullerene-Based n-type Thermoelectrics. *J. Mater. Chem. A*. **2017**, *5*, 21234-21241.

(43) Tada, A.; Geng, Y.; Wei, Q.; Hashimoto, K.; Tajima, K. Tailoring Organic Heterojunction Interfaces in Bilayer Polymer Photovoltaic Devices. *Nat. Mater.* **2011**, *10*, 450-455.

(44) Nakano, K., Chen, Y.; Xiao, B.; Han, W.; Huang, J.; Yoshida, H.; Zhou, E.; Tajima, K. Anatomy of the Energetic Driving Force for Charge Generation in Organic Solar Cells. *Nat. Commun.* **2019**, *10*, 1-10.

(45) Ade, H.; Hitchcock, A. P. NEXAFS Microscopy and Resonant Scattering: Composition and Orientation Probed in Real and Reciprocal Space. *Polymer* **2008**, *49*, 643-675.

(46)Gann, E.; Young, A. T.; Collins, B. A.; Yan, H.; Nasiatka, J.; Padmore, H. A.; Ade, H.; Hexemer, A.; Wang, C. Soft X-ray Scattering Facility at the Advanced Light Source with Real-Time Data Processing and Analysis. *Rev. Sci. Instrum*. **2012**, *83*, 045110.

(47) Liu, Y.; Zhao, J.; Li, Z.; Mu, C.; Ma, W.; Hu, H.; Jiang, K.; Lin, H.; Ade, H.; Yan, H. Aggregation and Morphology Control Enables Multiple Cases of High-Efficiency Polymer Solar Cells. *Nat. Commun*. **2014**, *5*, 1-8.

(48) Zhao, J.; Li, Y.; Yang, G.; Jiang, K.; Lin, H.; Ade, H., Ma, W.; Yan, H. Efficient Organic Solar Cells Processed from Hydrocarbon Solvents. *Nat. Energy* **2016**, *1*, 1-7.

(49) Ye, L.; Hu, H.; Ghasemi, M.; Wang, T.; Collins, B. A.; Kim, J.; Jiang, K.; Carpenter, J. H.; Li, H.; Li, Z.; McAfee, T.; Zhao, J.; Chen, X.; Lai, J. L. Y.; Ma, T.; Brédas, J.; Yan, H.; Ade, H. Quantitative Relations between Interaction Parameter, Miscibility and Function in Organic Solar Cells. *Nat. Mater*. **2018**, *17*, 253-260.

(50) Ye, L.; Li, S.; Liu, X.; Zhang, S.; Ghasemi, M.; Xiong, Y.; Hou, J.; Ade, H. Quenching to the Percolation Threshold in Organic Solar Cells. *Joule* **2019**, *3*, 443-458.

(51) Scholes, D. T.; Hawks, S. A.; Yee, P. Y.; Wu, H.; Lindmuth, J. R.; Tolbert, S. H.; Schwartz, B. J. Overcoming Film Quality Issues for Conjugated Polymers Doped with F4TCNQ by Solution Sequential Processing: Hall Effect, Structural, and Optical Measurements. *J. Phys. Chem. Lett.* **2015**, *6*, 4786-4893.

(52) Wang, Y.; Zhu, Q.; Naveed, H. B.; Zhao, H.; Zhou, K.; Ma, W. Sequential Blade‐Coated Acceptor and Donor Enables Simultaneous Enhancement of Efficiency, Stability, and Mechanical Properties for Organic Solar Cells. *Adv. Energy Mater.* **2020**, *10*, 1903609.

(53) Wei, P.; Dong, J. H. Oh, G.; Bao, Z. 2-(2-Methoxyphenyl)-1,3-Dimethyl-1H-Benzoimidazol-3-ium Iodide as a New Air-Stable n-Type Dopant for Vacuum-Processed Organic Semiconductor Thin Films. *J. Am. Chem. Soc*. **2012**, *134*, 3999-4002.

(54) Naab, B. D.; Himmelberger, S.; Diao, Y.; Vandewal, K.; Wei, P.; Lussem, B.; Salleo, A.; Bao, Z. High Mobility n-Type Transistors Based on Solution-Sheared Doped 6, 13-Bis (triisopropylsilylethynyl) Pentacene Thin Films. *Adv. Mater*. **2013**, *25*, 4663-4667.

(55) Li, T.; Dai, S.; Ke, Z.; Yang, L.; Wang, J.; Yan, C.; Ma, W.; Zhan, X. Fused Tris (thienothiophene)-Based Electron Acceptor with Strong Near-Infrared Absorption for High-Performance As-Cast Solar Cells. *Adv Mater*. **2018**, *30*, 1705969.

(56) Kim, J.; Gadisa, A.; Schaefer, C.; Yao, H.; Gautam, B. R.; Balar, N.; Ghasemi, M.; Constantinou, L.; So, F. O'Connor, B. T.; Gundogdu, K.; Hou, J.; Ade, H. Strong Polymer Molecular Weight-Dependent Material Interactions: Impact on The Formation of The Polymer/Fullerene Bulk Heterojunction Morphology. *J. Mater. Chem. A*. **2017**, *5*, 13176-13188.

(57) Ye, L.; Collins, B.; Jiao, X.; Zhao, J.; Yan, H.; Ade, H. Miscibility-Function Relations in Organic Solar Cells: Significance of Optimal Miscibility in Relation to Percolation. *Adv. Energy Mater*. **2018**, *8*, 1703058.

(58)Hexemer, A.; Bras, W.; Glossinger, J.; Schaible, E.; Gann, E.; Kirian, R.; MacDowell, A.; Church, M.; Rude, B.; Padmore, H. A SAXS/WAXS/GISAXS Beamline with Multilayer Monochromator. *J. Phys. Conf. Ser*. **2010**, *247*, 012007.

(59) Wang, C.; Lee, D. H.; Hexemer, A.; Kim, M. I.; Zhao, W.; Russell, T. P. Defining The Nanostructured Morphology of Triblock Copolymers Using Resonant Soft X-Ray Scattering. *Nano Lett.* **2011**, *11*, 3906-3911.

(60) Liu, F.; Brady, M. A.; Wang, C. Resonant Soft X-Ray Scattering for Polymer Materials. *Eur. Polym. J.* **2016**, *81*, 555-568.

(61) Yurash, B.; Cao, D. X.; Brus, V. V.; Leifert, D.; Wang, M.; Dixon, A.; Seifrid, M.; Mansour, A. E.; Lungwitz, D.; Liu, T.; Santiago, P. J.; Graham, K. R.; Koch, N.; Bazan, G. C.;

Nguyen, T. -Q. Towards Understanding The Doping Mechanism of Organic Semiconductors by Lewis Acids. *Nat. Mater.* **2019**, *18*, 1327-1334.

(62) Yan, H.; Ma, W. Making Weak Dopants Strong. *Nat. Mater.* **2019**, *18*, 1269-1270.

Table of Contents